RESEARCH ARTICLE

CrossMark

Manganese oxide nanoparticles supported nitrogen-doped graphene: a durable alkaline oxygen reduction electrocatalyst

Ila Jogesh Ramala Sarkar[1] · Shaik Gouse Peera[1] · Raghuram Chetty[1]

Abstract

Manganese oxide-based nitrogen-doped reduced graphene oxide (MnO/N-rGO) electrocatalyst was developed by a simple sol–gel process with aqueous $KMnO_4$ and sucrose by adding nitrogen-doped reduced graphene oxide. The physical characterizations were systematically evaluated by X-ray diffraction, field emission scanning electron microscope, transmission electron microscope, and X-ray photoelectron spectroscopy. The electrochemical and oxygen reduction properties of the electrocatalyst and support were studied by employing cyclic voltammetry and linear sweep voltammetry techniques on a rotating-disk electrode in alkaline (0.1 M KOH) solution and compared with commercial Pt/C catalysts. The synthesized catalyst possesses a high oxygen reduction activity and the rotating ring-disk electrode results illustrate a 3.8 e^- transfer process. Stability tests performed for 10,000 potential cycles exhibited that the MnO/N-rGO catalyst is more durable than Pt/C catalyst. MnO/N-rGO as cathode catalyst in a single alkaline fuel cell studies gave a peak power density of 44 mW cm^{-2} at 40 °C. Durability by accelerated stress test (AST) in fuel cell mode demonstrated MnO/N-rGO as alternative hybrid cathode catalyst which has excellent stability and durability of 67% more than commercial Pt/C.

Graphical Abstract
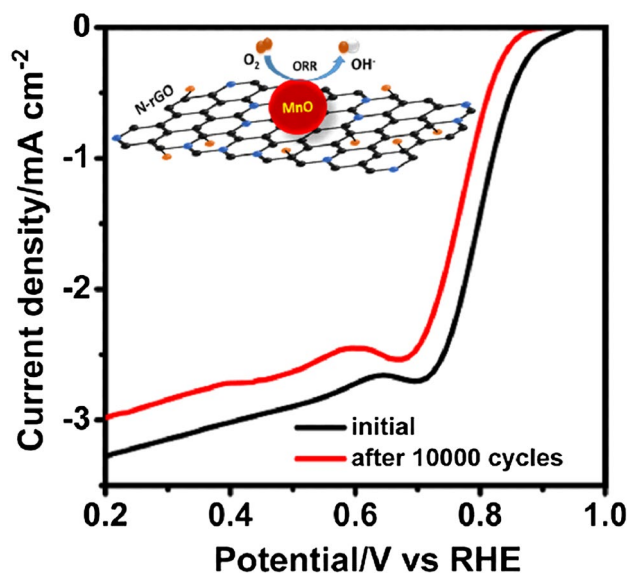
1 Introduction

Fuel cells are considered as ideal, efficient power sources of renewable energy conversion devices due to their higher efficiency in terms of deliverable power density and nearly zero emission [1]. Especially, proton exchange membrane fuel cells (PEMFCs) have been recognized as most possible alternative for transportation and stationary applications [2]. However, the use of Pt/C-based catalysts makes PEMFCs expensive and hinders its successful commercialization [1, 3]. Moreover, the durability of Pt/C catalysts is another important factor to be considered for its reliability in terms of long-term operations under the aggressive acidic environment, exists in the PEMFCs [4]. In this context, alkaline membrane fuel cells (AMFCs) possess advantages over PEMFCs, including faster reactions kinetics due to the highly alkaline conditions and offers opportunities of using inexpensive/non-precious metal nanoparticles as catalyst [5]. Hence, cost of the AMFCs could be reduced significantly than the PEMFCs. However, other than the low cost; high catalytic activity and durability of the cathode catalyst are the other two parameters which must be fulfilled by any catalyst developed especially in real fuel cell operating conditions.

Cathodic oxygen reduction reaction (ORR) is considered as sluggish and determines the overall power efficiency of an operating AMFCs, besides hydroxyl ion conductivity of the alkaline membrane [6, 7]. The commonly used catalyst for efficient ORR is Pt-supported carbon (Pt/C) [8]. A broad range of alternative catalysts for cathodic ORR based on (i) non-precious metals, (ii) metal oxides, (iii) nitrogen-coordinated metal on carbon, and (iv) metal-free doped carbon materials have been actively pursued in the literature [4, 9–11]. Among these, metal oxide catalysts have gained a prominence due to their ease and versatility of preparation, high activity, wide stability range, and environmental abundance. During the past decades, detailed studies have been carried out with metal oxides supported on carbon like MnO_2, Mn_2O_3, Mn_3O_4, Fe_3O_4, CoO, and Co_3O_4 [12–19].

On the other hand, developing stable carbon support also plays a major role on the durability of the supported catalysts. Generally, utilized carbon black supports possess low graphitized character and hence prone to carbon corrosion [9–11]. Hence, developing stable carbon support also decides the long life of the fuel cell device. Various graphitized nanostructured carbon materials such as carbon nanotubes (CNTs), spherical carbon, graphitic carbon nanofibers (CNFs), and meso/macroporous carbon materials have been developed to increase the durability of the supported catalysts [20–26]. Recently, graphene, a two-dimensional carbon material with unique mechanical and electronic properties, have come into sight as an alternative catalyst support due to its high surface area, high electrical conductivity, and graphitic nature, which offers as a best support material for nanoparticle deposition and dispersion [27]. In addition, several reports suggest that nitrogen doping on graphene offers several advantages, such as (i) N-doped sites serve as catalytic centers for ORR and hence considered as a metal-free catalysts, (ii) N doping helps as anchoring sites for metal nanoparticles and facilitates the uniform dispersion of the metal nanoparticles, (iii) N doping enhances metal-support interaction through charge transfer across graphene–metal interface and (iv) N doping also act as a tapping sites to help prevent metal detachment and hence effectively prevents the agglomeration of supported metal nanoparticles under real fuel cell operating conditions [16, 28, 29].

Nitrogen doping to carbon matrix is an effective way of activating the π electrons of carbon. Quantum mechanics calculations revealed that the electron accepting/donating ability of heteroatom dopant creates net positive/negative charges on the adjacent carbon atoms in the carbon crystal lattice to facilitate oxygen reduction. Moreover, N doping enhances the charge delocalization of adjacent carbon atoms by inducing different charge and spin density. Due to the electronegativity difference between C and N, the C–N bond polarization occurs and this induces partial positive charges on the adjacent carbons atoms. These partially positive charged carbon atoms facilitate oxygen adsorption and its subsequent reduction making N-doped carbons active towards electrocatalytic reactions [30, 31]. In contrast to the work reported by Sheng et al. [30] and Gong et al. [31], in this study, metal oxide nanoparticles were deposited on to an N-rGO support, to take the synergistic advantage of metal oxide nanoparticles with the N-rGO support, towards ORR activity in alkaline medium.

Among the metal oxide electrocatalysts studied, manganese oxide as cathode ORR catalyst material has gained considerable attention due to their low cost, environmentally benign nature rich in chemical and electrochemical properties. Zhang et al. synthesized a composite catalyst ($RGO-MnO_2$) by directly growing manganese dioxide (MnO_2) on RGO sheets via chelation-mediated aqueous method at low temperature [12]. Feng et al. developed a novel ORR catalyst by nucleation and growth of Mn_3O_4 nanoparticles on graphene oxide (GO) sheets interconnected by electrically conducting multi-walled carbon nanotubes (MWCNTs) [32]. Recent report by She et al. demonstrated one-step microwave-assisted synthetic route for the fabrication of Mn_3O_4 nanoparticles on reduced graphene oxide (Mn_3O_4@rGO) nanocomposites [33]. Li et al.

developed transition metal (Fe, Co, Ni, and V) ions-doped MnO_2 nanosheets (MONS), grown on the internal surface of macro porous carbon derived from luffa sponge fibers as electrocatalyst for oxygen reduction reaction (ORR) [34]. Recently, Arunchander et al. hydrothermally synthesized MnO nanoparticles supported on N-graphene as a durable ORR catalyst in a two-step process. However, the hydrothermally synthesized MnO nanoparticle resulted in large particle size of 100–130 nm and a power density of only 13 mW cm^{-2} in a real fuel cell condition was obtained [35].

In this work, manganese oxide (MnO) nanoparticles were synthesized by a simple sol–gel route and are supported on N-doped reduced graphene oxide (MnO/N-rGO) as a durable ORR catalyst in alkaline electrolyte. The sol–gel synthesis route is generally simple, facile, and the nanoparticles synthesized by sol–gel routes possess distinctive properties which are not found from materials produced by more traditional precipitation/hydrothermal process. Graphene oxide (GO) is prepared from graphite powder by Hummers method and the N doping to GO was carried out using melamine as a nitrogen source. The synthesized MnO/N-rGO catalyst was subjected to various physico-electrochemical characterizations. The performance of the catalyst towards ORR was evaluated in alkaline media and an accelerated durability test was performed to assess the catalyst stability. In addition, fuel cell performance of the MnO/N-rGO catalyst was evaluated and compared to commercial Pt/C catalyst.

2 Experimental

2.1 Reagents and chemicals

Graphite powder (~ 60 mesh size) and melamine ($C_6H_3N_6$) were purchased from Loba Chemie, India. Sulphuric acid (H_2SO_4), potassium permanganate ($KMnO_4$), H_2O_2, sucrose, and potassium hydroxide (KOH) were obtained from Merck, India. Sodium nitrate ($NaNO_3$) was obtained from RANKEM. Ethanol was procured from Hayman limited. Commercial Pt/C (40 wt% Pt on carbon) was obtained from Alfa Aesar. Ammonium-type anion exchange membrane (AHA-NEOSEPTA, thickness 50 μm) was obtained from ASTOM Corporation, Japan. Nafion (5 wt%) ionomer solution was procured from Sigma–Aldrich and Fumion-FAA-3 (10 wt%) ionomer solution was purchased from Fumatech, Germany. High-purity water (18.2 MΩ cm) used for all experiments was produced by a MilliQ system.

2.2 Synthesis of graphene oxide and nitrogen-doped reduced graphene oxide

Graphene oxide was synthesized from graphite powder according to the conventional Hummer's method [36]. Nitrogen-doped graphene oxide (N-rGO) was synthesized

by heat treating mixture of graphene oxide and melamine (as the N source). Briefly, 400 mg of graphene oxide was mixed with 30 ml of MilliQ water and sonicated for 30 min. To this slurry, required amount of melamine with an optimized mass ratio of 1:10 (graphene oxide and melamine) was added and further sonicated for 2 h. The obtained slurry was dried overnight in hot air-oven at 80 °C to remove water. The resultant mixture was then grounded to fine powder and annealed in tubular furnace at 900 °C for 1 h under nitrogen atmosphere with a heating ramp of 5 °C min^{-1}.

2.3 Synthesis of manganese oxide on nitrogen-doped reduced graphene oxide composite (MnO/N-rGO)

Manganese oxide nanoparticles supported on N-rGO was synthesized by a simple sol–gel method. In a typical procedure, 1.5 g of $KMnO_4$ solution (25 ml) was added into an as-prepared N-rGO of 200 mg and sucrose suspension (4.78 g in 10 ml) as shown in Scheme 1. The mixture was subjected to quick agitation and then let stand to form a gel. A dark monolithic gel was obtained which was dried overnight in hot air oven at 70 °C. The residue was washed with MilliQ water, centrifuged, dried at 70 °C overnight, and grounded to get fine powder. The sample was then heat treated in a tubular furnace at an optimized temperature of 800 °C for 1 h under N_2 atmosphere. During the high-temperature treatment the initial xerogel structure collapsed and transformed into manganese oxide nanoparticles (MnO) [37]. Heat-treated sample was grounded to get the final catalyst, labeled as MnO/N-rGO-800. For the synthesis of MnO catalyst, similar process is followed, in which aqueous $KMnO_4$ solution is poured to the aqueous mixture of sucrose. The resulting mixture was subjected to calcination at 800 °C under nitrogen atmosphere to get the MnO catalyst as shown in Scheme 1.

2.4 Physico-chemical characterization

The phase structures for all of the catalysts were obtained by powder X-ray diffraction (XRD) patterns (Model: Bruker AXS D8 Discover XRD) employing CuKα radiation of wavelength 1.54 Å. The morphological images of the catalysts and mapping of the elements were studied using a field emission scanning electron microscope (FE-SEM, Hitachi S 4800). The Mn nanoparticles distribution on the N-rGO was analyzed using a high-resolution transmission electron microscope (TEM, JEOL JEM-2100) with an acceleration voltage of 200 keV. For these measurements, the samples were suspended in ethanol with ultrasonic dispersion for 2 min. Subsequently, a drop of the suspension was casted on a carbon-coated copper grid and allowed to dry prior to the TEM analysis. To ensure the presence of nitrogen
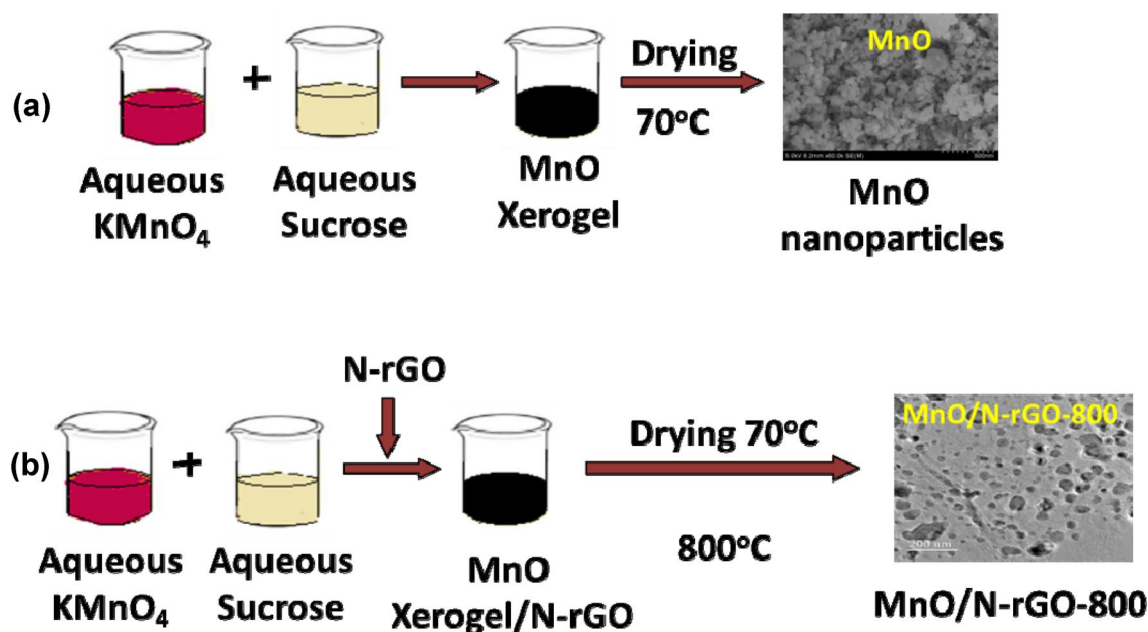
Scheme 1 **a** Represents manganese oxide (MnO) synthesis and **b** represents synthesis of MnO/N-rGO-800 catalyst

and the interaction of the Mn nanoparticles with the support material, X-ray photoelectron spectroscopy (Thermo Fisher Scientific, ESCALAB 250 XPS system) was used with a monochromated Al Kα source at 15 keV and 150 W system.

2.5 Electrochemical measurement

The electrochemical performance of the catalysts was measured using a potentiostat/galvanostat (CH instruments) and rotating-disk electrode (RDE) apparatus at 25 °C in a three-electrode electrochemical cell. A glassy carbon (GC) electrode (geometric area: 0.071 cm^2) was used as the working electrode substrate for electrochemical studies, whereas Pt coil was used as the counter electrode and Ag/AgCl electrode served as the reference electrode. A catalyst ink was obtained by adding 5 mg catalyst and 10 wt% Nafion solution (10 μl of 5 wt% Nafion solution) to 1 ml of water:ethanol mixture followed by ultrasonication for 1 h. Prior to catalyst coating, GC electrode was mirror polished using 0.5 μm alumina slurry and then cleaned ultrasonically with ethanol and MilliQ water to obtain a clean and smooth electrode surface. A 10 μl of the dispersed suspension was drop casted onto the GC electrode to obtain the desired catalyst loading of 850 μg cm^{-2}. For comparison, commercial Pt/C (20 wt%) with the catalyst loading of 40 μg cm^{-2} was dropped cast onto the GC electrode and further analyzed for electrochemical properties.

Cyclic voltammograms (CVs) were studied at a scan rate of 50 mV s^{-1} in 0.1 M KOH aqueous solution saturated with either N$_2$/O$_2$. Linear sweep voltammetry (LSV) for
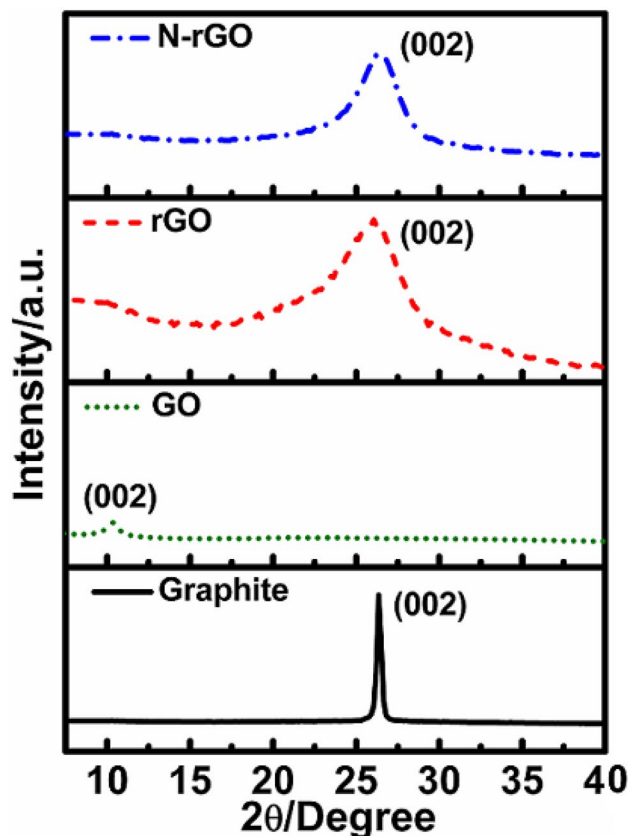

Fig. 1 XRD patterns of graphite, GO, rGO, and N-rGO

ORR activity measurements was performed using a RDE in aqueous 0.1 M KOH saturated with O_2 at a scan rate of 10 mV s^{-1} at different rotational speeds. For electrochemical stability measurements of the catalysts, CVs were repeated for 10,000 potential cycles between 0 and 1.2 V versus RHE and LSVs were recorded before and after the potential cycles to assess the stability of the catalysts. Rotating ring-disk electrode (RRDE) of the catalyst was performed with GC electrode (5 mm diameter) and a Pt ring (Pine Instruments) to obtain percentage peroxide yield and number of electron transferred during the ORR process. For RRDE working electrode, a 10 µl of catalyst slurry was drop casted onto the GC electrode and allowed to dry at room temperature. All potentials were normalized with pH of the electrolyte and finally converted with respect to reversible hydrogen electrode (RHE) ($E_{RHE} = E$ (Ag/AgCl) + (0.059 × pH)) for convenience.

2.6 Fuel cell studies and durability evaluation

Commercial SGL DC-35 gas diffusion layer was used as a substrate for the electrodes. A well-dispersed cathode catalyst ink was prepared by mixing calculated amount of MnO/N-rGO-800 catalyst with MilliQ water, ethanol, and Fumion-FAA-3 (10 wt%) ionomer solution followed by ultrasonication. To obtain a catalyst-coated substrate for cathode, the as-prepared ink was coated onto surface of carbon fiber paper using a paint brush. The MnO/N-rGO-800 loading in the catalyst layer was ~6 mg cm^{-2}. For anode catalyst preparation, the ink was made by mixing Pt/C (40 wt%) also with same proportion of above solvents and maintained a catalyst loading of 2.5 mg cm^{-2}. For comparison, both anode and cathode catalyst were made with Pt/C (40 wt%) with the catalyst loading 2.5 mg cm^{-2}. Prior to membrane electrode assembly (MEA), all electrodes were activated by dipping the electrodes with 0.1 M KOH solution for 12 h, followed by copious washing with MilliQ water to remove excess KOH and drying at 40 °C. As-purchased alkaline membrane (from ASTOM Corporation, Japan, AHA-NEOSEPTA, thickness 50 µm) was also treated with 0.1 M KOH solution for 24 h, followed by repeated wash with MilliQ water. Anode catalyst-coated substrate, membrane, cathode catalyst-coated substrate were assembled together and the MEA was fabricated with the help of hot press at 40 °C for 3 min with the compression force of 10 kg cm^{-2}. The performance of MEAs was obtained using
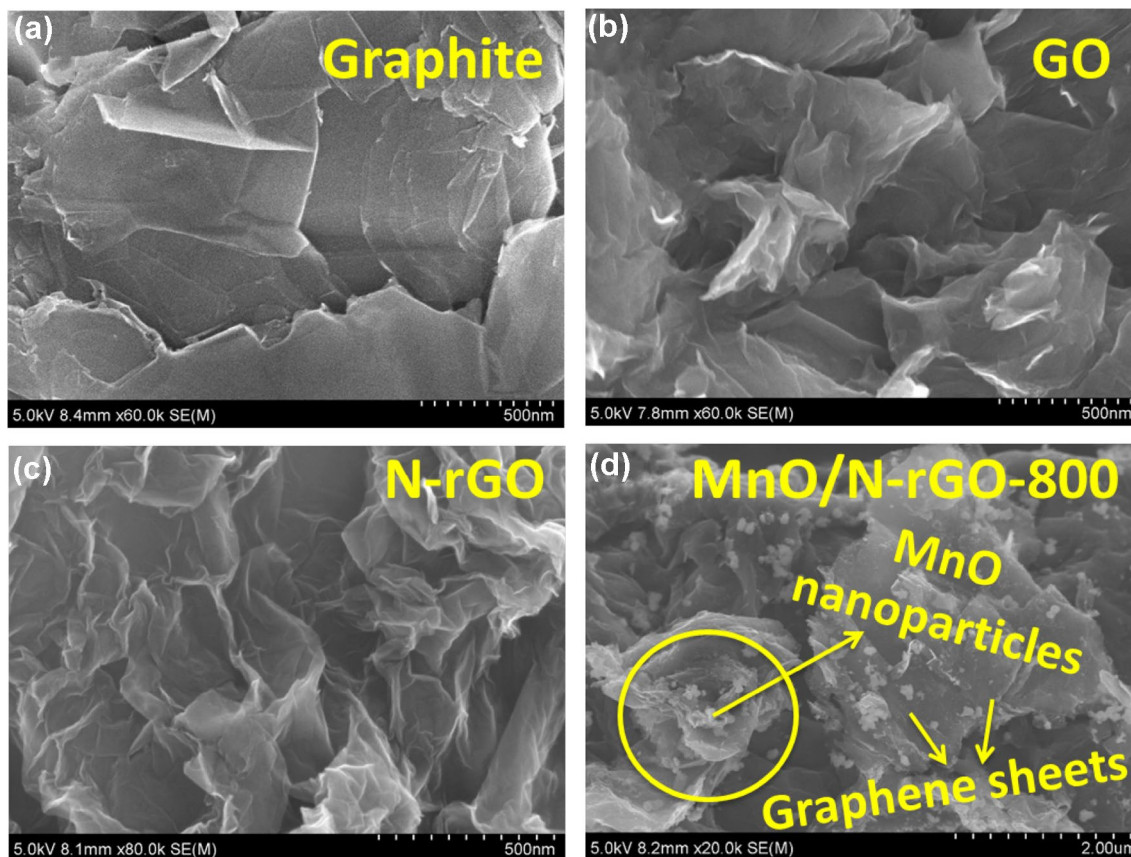

Fig. 2 FE-SEM images of **a** graphite, **b** GO, **c** N-rGO, and **d** MnO/N-rGO-800

a conventional 4 cm^2 fuel cell test fixture with a parallel serpentine flow field machined on graphite plates. After equilibration, the single cells *i–v* characteristics were obtained at 40 °C and ambient pressure using potentiostat (Biologic Science Instrument: SP-150) with gaseous H$_2$ (100% RH) and gaseous O$_2$ (100% RH) to the anode and cathode of the AMFCs at a flow rate of 100 and 150 ml min^{-1}, respectively.

To evaluate the durability performance of MEAs, an accelerated stress test (AST) method was employed by holding the operating fuel cell at a higher cell voltage of 1.4 V for 30 s and then decreasing the cell voltage to 0.6 V for 2 min 30 s to complete a cycle [38]. This process was repeated for 50 cycles and fuel cell polarization curves were recorded before and after the cycling test to assess the durability of the MEAs.
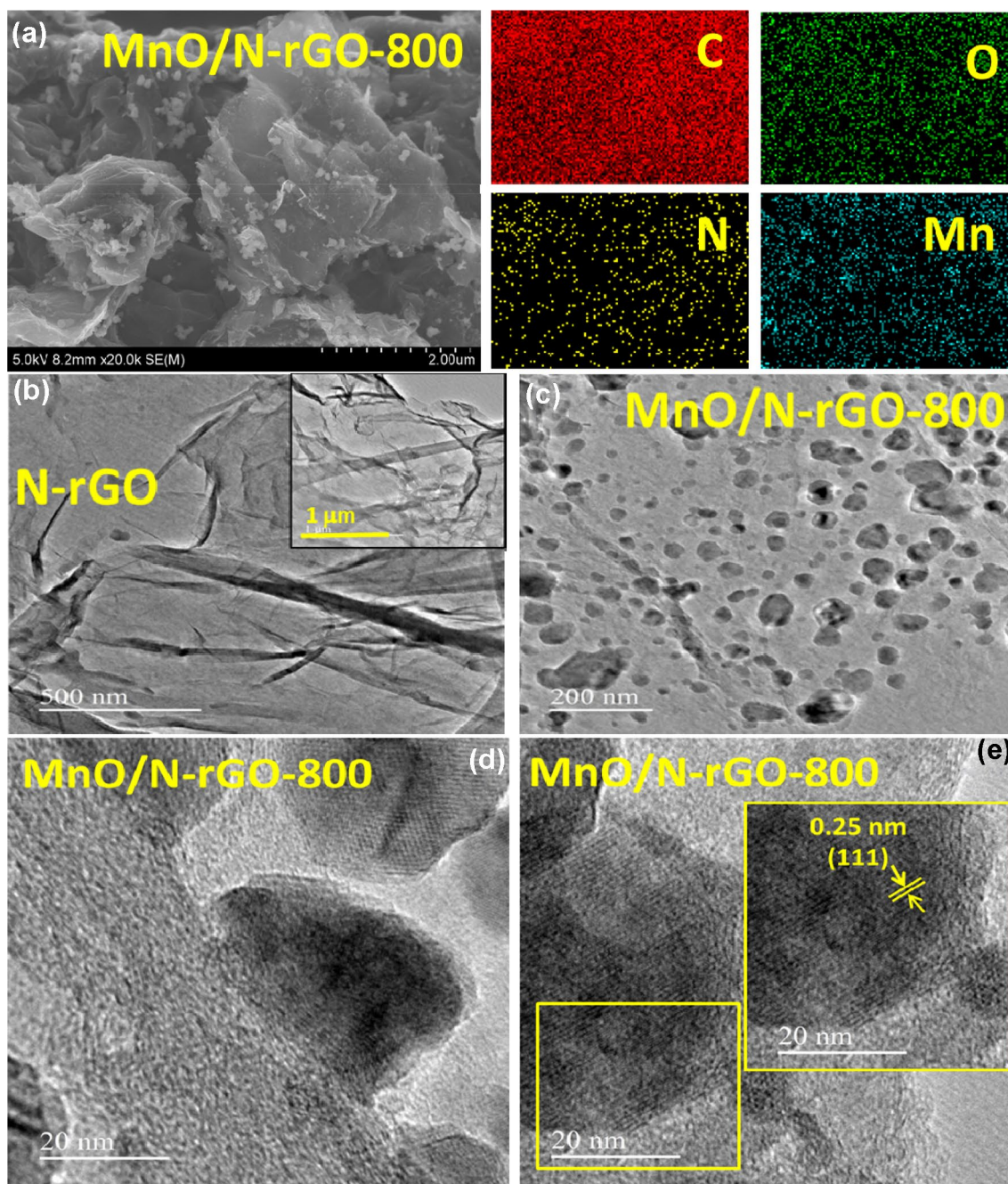
Fig. 3 **a** FE-SEM image and the corresponding elemental mappings of MnO/N-rGO-800, **b** TEM images of N-rGO at different magnifications and **c** TEM images of MnO/N-rGO-800 hybrid catalyst and **d, e** high-resolution TEM images of MnO/N-rGO-800 hybrid catalyst

3 Results and discussion

3.1 Physical characterization

Figure 1 shows the XRD patterns of graphite, graphene oxide (GO), and N-rGO. A sharp peak at 2θ value of 26° of graphite is attributed to (002) planes of crystalline hexagonal graphitic structure. The diffraction peaks were shifted to lower angles in case of GO sample, indicating the increased interlayer spacing and loss of crystallinity during the oxidation process. This is due to the introduction of various oxygen functional groups during the oxidation process, confirming the exfoliation of graphite structure by oxidation process. N doping to the GO was performed with melamine as nitrogen source. Melamine molecules adsorb on the surface of GO, which subsequently forms carbon nitride during the pyrolysis process. Further decomposition of the carbon nitride releases the N species in the vicinity and simultaneous removal of oxygen species from the GO, provides the active sites for insertion of N into the carbon matrix, giving N-rGO [21]. Hence, both N doping and reduction of GO to reduced graphene oxide occurs simultaneously during the pyrolysis process. This was further confirmed by the XRD diffraction (as shown in Fig. 1) patterns of N-rGO, which shifts to its original 2θ values of 26°. Figure 2 shows the SEM images of graphite, graphene oxide (GO), N-rGO, and MnO/N-rGO samples. Pristine graphite shows a clear flakelike structure (Fig. 2a). This flakelike structure exfoliates after oxidation process and loses its crystalline nature due to the increase interlayer spacing (Fig. 2b). In contrast, Fig. 2c, formation of clear graphene sheets is observed indicating a complete conversion of flake graphite to graphene sheets and confirming the successful synthesis of N-graphene sheets. Further, TEM measurements also confirm the clear formation of graphene sheets as discussed below. Figure 2d shows the SEM image of MnO/N-rGO-800, confirming the successful synthesis of MnO on N-doped reduced graphene sheets. SEM micrographs of as synthesized MnO nanoparticles are shown in Fig. S1 of Supporting Information, which mainly appears as agglomerates due to the absence of carbon-based support.

From Fig. 3a, which shows the EDX elemental mapping and the corresponding SEM image of MnO/N-rGO-800 catalyst confirms the successful doping of N and homogenous distribution of MnO nanoparticles on the surface of N-rGO. Figure 3b shows the TEM images of N-rGO at higher and lower magnifications. From the TEM images of MnO/N-rGO-800 catalyst shown in Fig. 3c, it is noticeable that MnO nanoparticles are evenly supported and distributed on the surface of graphene sheets. The average MnO nanoparticle size is found to be 20 nm from the TEM measurements. The HR-TEM images of MnO/N-rGO catalyst are shown

in Fig. 3d, e, wherein clear lattice fringes of MnO nanoparticles are seen in the inset of Fig. 3e and the noticeable d-spacing of 0.25 nm is attributed to the (111) plane of the MnO nanoparticle, which is one of the phases of MnO species in the MnO/N-rGO catalyst as observed from XRD patterns of MnO/N-rGO catalysts shown in Fig. 4.

Figure 4 shows the XRD patterns for MnO, MnO/N-rGO, and MnO/N-rGO-800 catalysts. From the diffraction patterns, it is clear that as synthesized MnO is amorphous in nature indicated by its broad and unresolved diffraction peaks in MnO and MnO/N-rGO, whereas the MnO/N-rGO-800 sample showed sharp diffraction patterns at 2θ values of 34.9, 40.53, 58.7, 69.9, and 74.03 characteristic of face-centered cubic (fcc) structure of MnO (111), (002), (022), (113), and (222) planes, indicating the crystalline nature of MnO nanoparticles. Further, the lattice constants are calculated from the diffraction patterns and are found to be $a = 4.4440$ Å, $b = 4.4440$ Å, and $c = 4.4440$ Å. The diffraction peaks and lattice constants when indexed with JCPDS data (PDF # 98-001-1336) features to pure MnO phase. Similar fcc structures of MnO nanoparticles at a temperature of 800 °C were reported by Arunchander et al. [35]. The crystallite size of MnO in MnO/N-rGO hybrid catalysts is calculated by considering the high intense peak (002) using Scherrer equation and is found to be ≈ 20 nm. The MnO nanoparticles loadings of ~40 wt% were achieved for all the catalysts as determined by the thermogravimetric analysis (shown in Fig. S2 of Supporting Information).

The electronic state and chemical nature of MnO/N-rGO-800 were elucidated with XPS measurements as shown in Fig. 5. The XPS survey spectra of N-rGO and MnO/N-rGO-800 show the presence of C, N, and O.
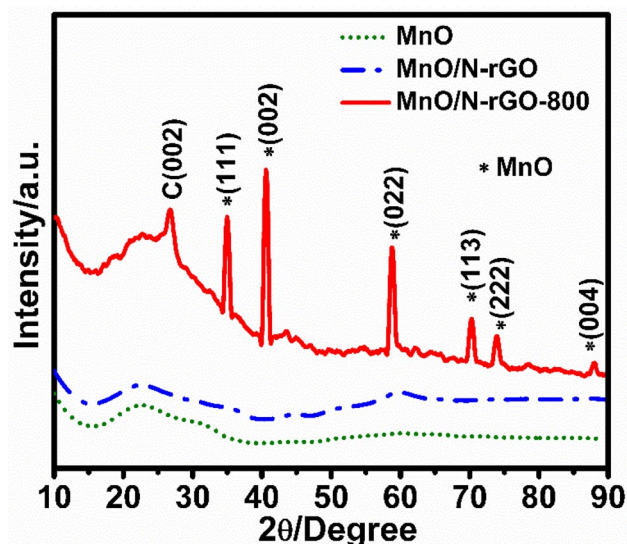

Fig. 4 XRD patterns of MnO, MnO/N-rGO, and MnO/N-rGO-800 catalysts, asterisks represent MnO phase

Atomic% of N was found to be 4.5%. Further, the high-resolution N spectra is recorded and deconvoluted into three different chemical states of N, namely pyridinic-N, pyrrolic-N, and graphitic-N at the binding energies of 398.13, 399.9, and 400.92 eV, respectively. It is reported that all the three chemical states of N are active for ORR, although the order of their activity varies [16, 28, 29]. The MnO/N-rGO-800 sample showed binding energy peaks of Mn at 642.12 and 653.55 eV corresponding to Mn ($2P_{3/2}$) and Mn ($2P_{1/2}$), respectively, indicating the presence of Mn in the catalyst. Moreover, the observed splitting width of 11.43 eV between Mn ($2P_{3/2}$) and Mn ($2P_{1/2}$) is in well agreement with earlier reports on MnO-based materials, confirming the deposition of MnO nanoparticles on the N-rGO support [39, 40].

3.2 Electrochemical characterization

The ORR activity of the catalysts synthesized in this study was investigated using RDE in alkaline solution of 0.1 M KOH at room temperature (25 °C) with CV and LSV techniques. Figure 6a shows the CVs of GO, rGO, and N-rGO catalysts in O_2 saturated 0.1 M KOH electrolyte recorded at a scan rate of 50 mV s^{-1}. A well-defined ORR reduction peak indicative of electrocatalytic oxygen reduction is observed for GO, rGO, and N-rGO in the region between 0.60 and 0.70 V. It is also observed that the ORR redox peak potentials shifts by 60 mV higher in case of N-rGO catalysts (0.70 V) when compared to GO (0.64 V) and 20 mV when compared to rGO (0.68 V). Figure 6b shows LSVs of GO and N-rGO catalysts recorded at 10 mv s^{-1} scan rate. The onset potential and half-wave potential are the important
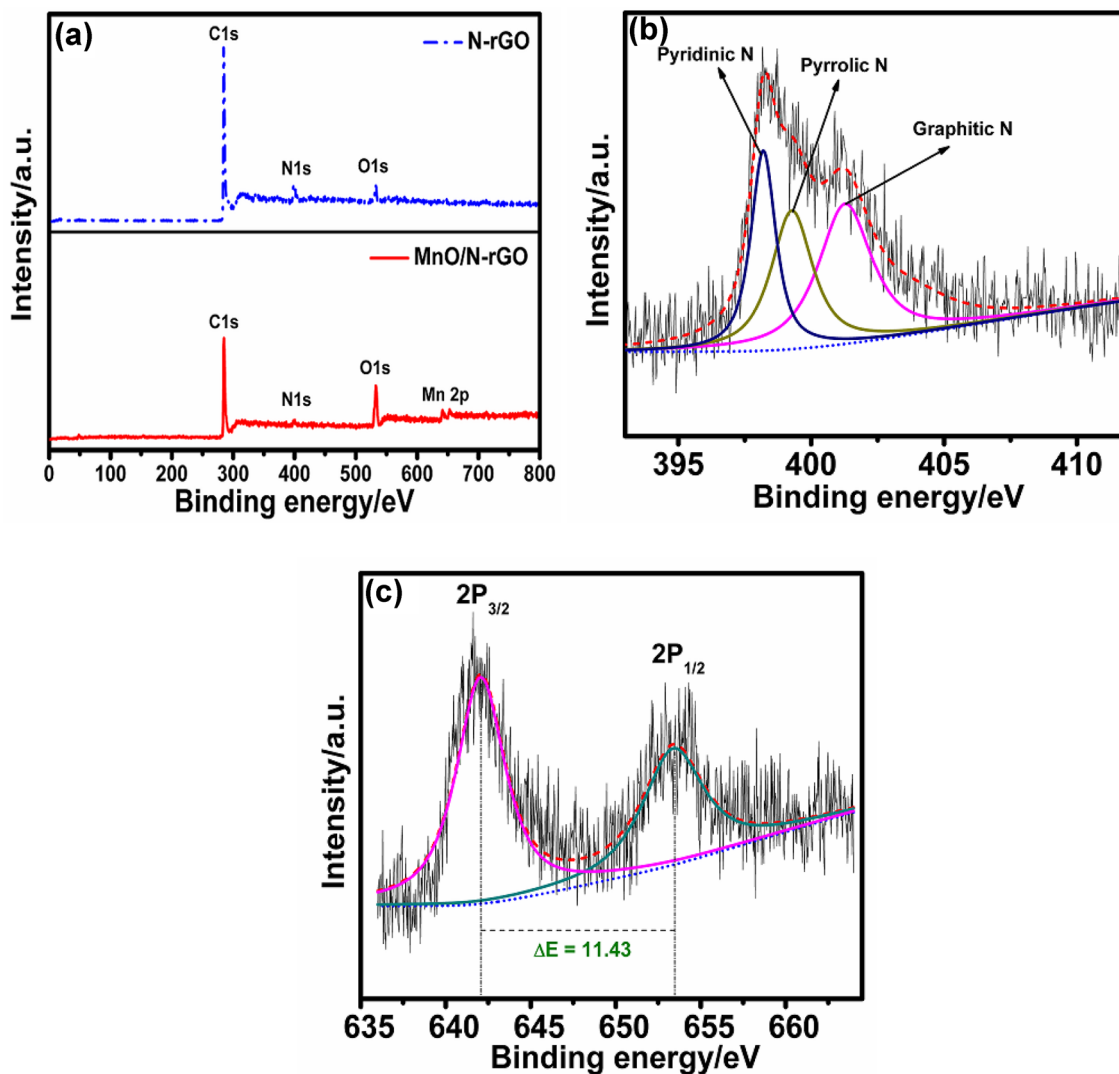

Fig. 5 **a** XPS survey spectra of N-rGO and MnO/N-rGO-800 hybrid catalysts, **b** deconvoluted N 1 s spectra, and **c** Mn 2p of MnO/N-rGO-800 catalyst

parameters to evaluate ORR activity of the electrocatalysts. The onset potentials and half-wave potentials of N-rGO, rGO, and GO catalysts are found to be 0.85, 0.80, and 0.78 V and 0.74, 0.71, and 0.70 V, respectively. The higher ORR redox potential of rGO in comparison to GO catalyst could be related to the restoration of sp2 carbons during thermal reduction, which leads to increased electrical conductivity and graphitization of rGO as evidenced from the XRD analysis (Fig. 1). Moreover, N-rGO showed higher activity both in terms of onset and half-wave potentials, when compared to rGO and GO catalysts. This clearly confirms the enhanced ORR activity of N-rGO catalyst, attributing the involvement of different forms of N (graphitic-N, pyridinic-N, and pyrrolic-N) in catalyzing ORR as reported in the earlier studies [16, 30, 31]. Hence, a synergistic enhancement

of ORR activity is anticipated with the deposition of MnO nanoparticles on the N-rGO catalyst [41].

Figure 7 shows the CVs and LSVs of MnO, MnO/N-rGO, and MnO/N-rGO-800 catalysts. From Fig. 7a, one can notice that the ORR reduction peaks shifts to higher potentials when MnO nanoparticles are deposited on the ORR active N-rGO support (MnO/N-rGO). The ORR redox peaks further positively shift to higher potentials for the heat-treated MnO/N-rGO-800 catalyst. Moreover, a significantly enhanced capacitance for MnO/N-rGO-800 catalyst is noticeable when compared to MnO, MnO/N-rGO catalysts. This could be due to the crystalline nature of MnO nanoparticles (as evident from the XRD studies, Fig. 4) which enhances the electronic conductivity and binding strength with N-doped graphene support for faster electron transfer kinetics between MnO and N-rGO. This clearly confirms the
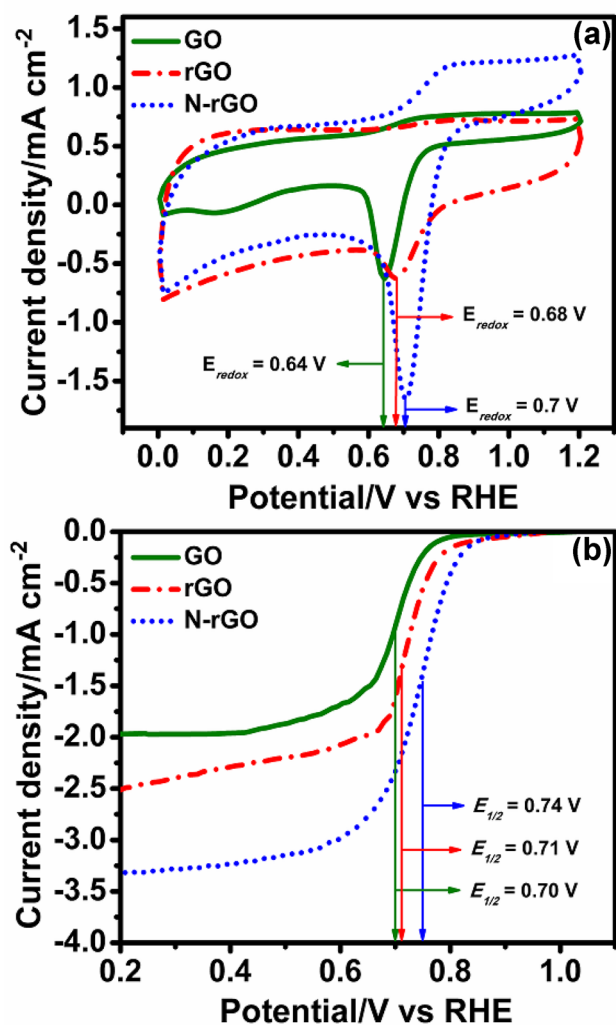
Fig. 6 **a** CVs and **b** LSVs of GO, rGO, and N-rGO recorded in O₂ saturated 0.1 M aqueous KOH electrolyte at a scan rate of 50 and 10 mV s⁻¹, respectively
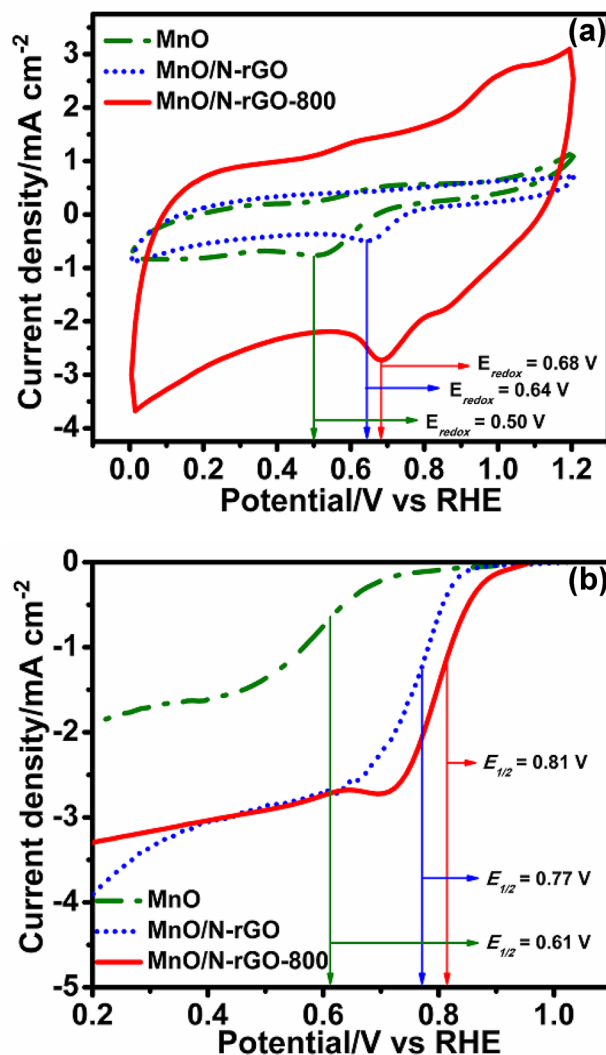
Fig. 7 **a** CVs and **b** LSVs of MnO, MnO/N-rGO, and MnO/N-rGO-800 recorded in O₂ saturated 0.1 M aqueous KOH electrolyte

definitive role of MnO nanoparticles and synergistic effect between metal oxide-nitrogen-doped graphene towards ORR [16, 33]. Moreover, the enhanced ORR activity and synergistic effect were further confirmed by LSV measurements as shown in Fig. 7b. The onset potentials for MnO, MnO/N-rGO, and MnO/N-rGO-800 are found to be at 0.75, 0.85, and 0.90 V and corresponding half-wave potentials are 0.61, 0.77, and 0.81 V, respectively. The amorphous nature and lower conductivity of MnO nanoparticles result in poor ORR activity for MnO catalyst [42]. To enhance the conductivity of the catalysts, MnO nanoparticles are supported on conducting N-rGO support (MnO/N-rGO) by means of physical mixing. This could enhance the electron transport from the support to the ORR active MnO nanoparticles and increase the electron density at the metal oxide-support junctions [43], as a result enhance the ORR kinetics as observed by the CV and LSV discussed above. However, physical mixing affords poor interaction between the MnO nanoparticles and N-rGO support, leaving behind a portion of MnO nanoparticles electrochemically inactive. Moreover, physical interaction of MnO nanoparticles with the N-rGO support always gives chances of detachment of supported MnO nanoparticles from the support, due to the weak adhesion of MnO nanoparticles with the N-rGO support. This leads to loss of active metal nanoparticles. To enhance the bonding strength and interaction between MnO and N-rGO support, the synthesis process was modified by adding N-rGO during the synthesis of MnO nanoparticles, in order to deposit the MnO nanoparticles *in situ*. This guarantees the uniform distribution of MnO nanoparticles on the N-rGO support as clearly observed by TEM measurements (Fig. 3c). Further, the resultant MnO/N-rGO catalyst is subjected to heat treatment at 800 °C. The high-temperature treatment increases the interaction between MnO nanoparticles and N-rGO support and hence effective conductivity of the final catalysts MnO/N-rGO-800 is guaranteed. Moreover, recent DFT theory calculations reveal that the N-doped graphene support enhances the diffusion of O_2 molecules by solid diffusion phenomenon to the metal ORR active sites [44, 45]. Hence, due to the synergistic effect of N-doped graphene and ORR active MnO nanoparticles, an enhanced ORR activity is anticipated for MnO/N-rGO-800 catalysts. This hypothesis is clearly evidenced from the electrochemical measurements (CVs and LSVs), where the MnO/N-rGO-800 catalysts presented the best electrocatalytic properties compared to N-rGO, MnO and MnO/N-rGO catalysts.

Figure 8 shows the ORR comparison plot of MnO/N-rGO-800 and the state-of-the-art Pt/C catalyst (with Pt loading of 60 µg cm^{-2}). It is noticed that, the half-wave potential for Pt/C catalyst is only 30 mV higher in relation to the MnO/N-rGO-800 hybrid catalyst. The steady-state limiting current densities of around 3.4 and 4.3 mA cm^{-2} are obtained for MnO/N-rGO-800 and Pt/C catalysts,

respectively. However, the obtained ORR activity of the synthesized MnO/N-rGO-800 catalyst is appreciable as a low-cost non-precious metal catalyst and shows its potential application towards the ORR due to the synergistic effect of N-rGO support and MnO nanoparticles forming active ORR centers. This encourages the use of MnO/N-rGO-800 as a possible cost effective alternate ORR electrocatalyst for the alkaline fuel cell cathode reaction.

In addition, the electro-kinetics of N-rGO, MnO/N-rGO, and Pt/C catalysts are examined by recording the hydrodynamic voltammograms at different rotations (800, 1200, 1600, 2000, and 2400 rpm) and are shown in Fig. 9a–c. The ORR current of all the catalysts increased with increasing rotation speed of the electrode, due to the shortened diffusion distance of the reactants between the electrode and electrolyte at high rotation speeds. Number of electrons involved during the ORR is generally determined from Koutecky–Levich (K–L) plot. The K–L plot, which is a plot of the inverse of current density (j^{-1}) as a function of the inverse of the square root of the rotation rate ($\omega^{-1/2}$) is obtained from Eqs. (1) and (2) and is used for the calculation of the number of electrons involved in the ORR [7].

$$i_d = B\omega^{1/2} \tag{1}$$

$$B = 0.2nFC_{O_2}D_{O_2}^{2/3}\vartheta^{-1/6} \tag{2}$$

where i_d is the diffusion controlled limiting current density, n is the number of electrons exchanged per O_2 molecule, F is the Faraday constant (96,485 C mol^{-1}), C_{O_2} is the bulk oxygen concentration in the electrolyte (1.22×10^{-6} mol cm^{-3}), D_{O_2} is the diffusion coefficient of molecular oxygen
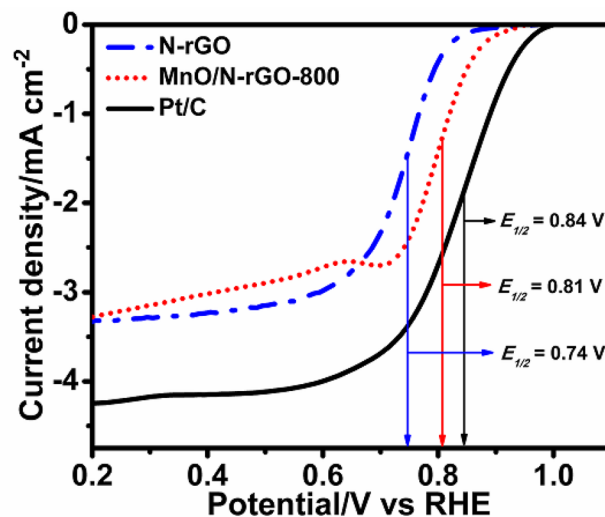

Fig. 8 Linear sweep voltammograms comparing N-rGO, MnO/N-rGO-800, and commercial Pt/C recorded in O_2 saturated 0.1 M aqueous KOH electrolyte at a scan rate of 10 mV s^{-1}

$(1.93 \times 10^{-5}$ cm^2 s^{-1}), ϑ is the kinematic viscosity of the electrolyte (0.01 cm^2 s^{-1}), ω is the rotations of the disk expressed in rpm ($\omega = 2\pi N$, N is the linear rotation speed), and 0.2 is a constant used when ω is expressed in rotations per minute. From the K–L plots, one can observe a good linearity and parallelism indicating first-order reaction kinetics

for all the catalysts. The number of electrons calculated from the slopes of the K–L plots for the catalysts N-rGO, MnO/N-rGO-800, and Pt/C was found to be 3.7, 3.8, and 3.9, which demonstrates a dominant 4-electron transfer process during the ORR. To further verify the ORR pathway of MnO/N-rGO-800 and Pt/C catalyst, rotating ring-disk electrode
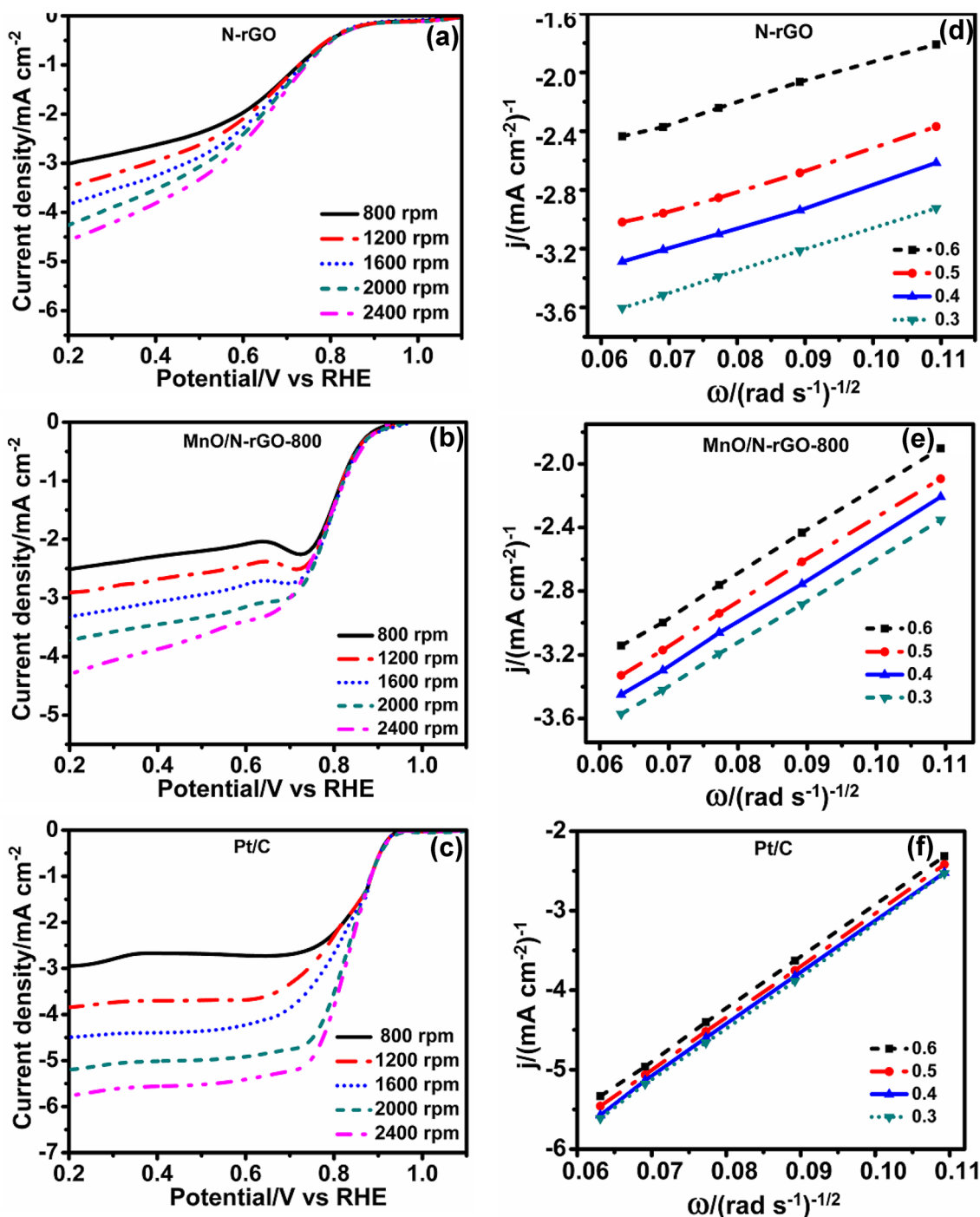
Fig. 9 **a–c** Linear sweep voltammograms of N-rGO, MnO/N-rGO-800, and Pt/C at different rotational rates and **d–f** corresponding K–L plots at different potentials of N-rGO, MnO/N-rGO-800, and Pt/C, respectively
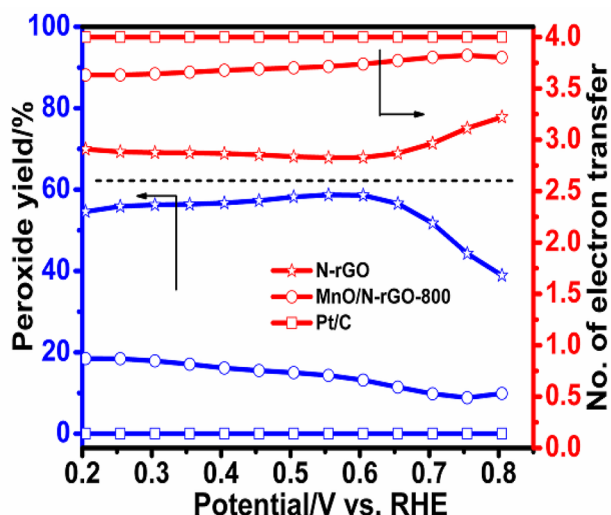
Fig. 10 Number of electron transferred and peroxide generated during ORR process of N-rGO, MnO/N-rGO-800, and Pt/C in O_2 saturated 0.1 M aqueous KOH electrolyte at a rotational rate of 1600 rpm

(RRDE) measurements as shown in Fig. 10 was performed and formation of peroxide species (HO^{2-}) are monitored. The percentage peroxide yield and the number of electrons transferred (n) are calculated by the following Eqs. (3) and (4):

$$\%H_2O_2 = 200 \times \frac{I_r/N}{I_d + I_r/N} \tag{3}$$

$$n = 2 \times \frac{2I_d}{I_d + I_r/N} \tag{4}$$

where I_d is the disk current, I_r is the ring current, and N is the current collection efficiency of Pt ring. The calculated number of electron transferred during the ORR process is found to be 3.8 and 3.9 for MnO/N-rGO-800 and Pt/C catalysts. The percentage peroxide yields are found to be 18 and 0.02% for MnO/N-rGO-800 and Pt/C, respectively. Arunchander et al. reported that MnO-based catalyst yield around 25% peroxide during ORR process [35].
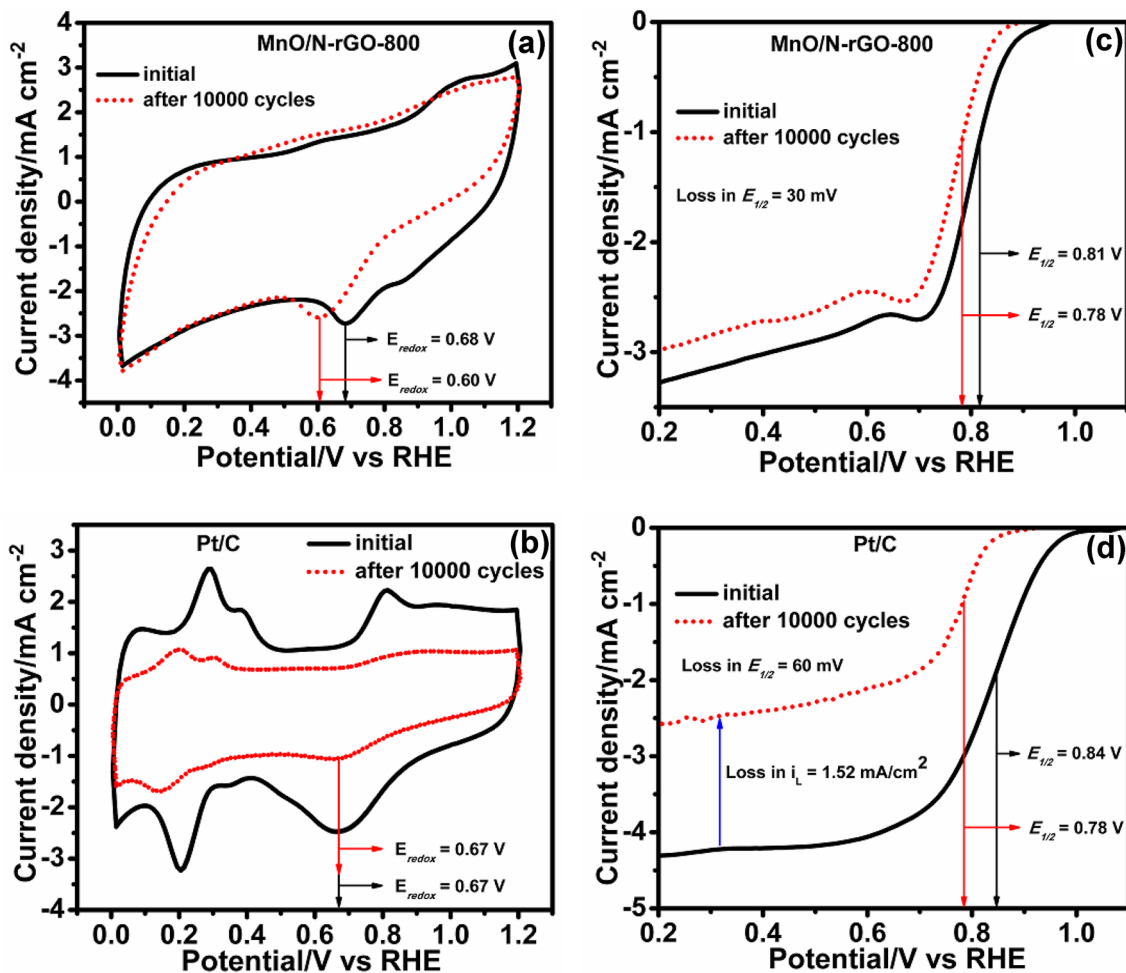
Fig. 11 CV of **a** MnO/N-rGO-800 and **c** commercial Pt/C catalyst; LSV of **b** MnO/N-rGO-800 hybrid catalyst and **d** commercial Pt/C catalyst. Plots are shown before and after durability test up to 10,000 potential cycles recorded in O_2 saturated 0.1 M aqueous KOH electrolyte. LSVs were conducted at a scan rate of 10 mV s^{-1} and rotational rate of 1600 rpm

In addition to the ORR activity of the catalyst, the long-term durability is also a key requirement for any developed catalyst as it has to sustain harsh environments during the real operation of the fuel cells. The durability of MnO/N-rGO-800 and Pt/C catalysts was evaluated by repeating potentiodynamic cycling tests by cycling the potential of working electrodes between 0 and 1.2 V for 10,000 cycles in an O_2 saturated aqueous 0.1 M KOH at room temperature, as shown in Fig. 11. The ORR behavior of the catalysts was assessed by recording the CVs and LSVs before and after 10,000 potential cycles which is a measure of the catalyst stability and degradation. The half-wave potentials of MnO/N-rGO-800 and Pt/C catalyst decreased by 30 and 60 mV when compared with their initial half-wave potentials. However, in case of Pt/C catalyst, charge associated with the OH adsorption/desorption and half of the limiting current are lost after the durability test, indicating its poor stability when compared with the MnO/N-rGO-800 catalyst. The salient improvement of MnO/N-rGO-800 catalyst towards ORR activity solely depends on the synergetic effect of N-rGO and MnO nanoparticles which provides strong metal-support interaction thereby enhancing the ORR activity and durability of the catalyst. This is ascertained by the durability investigation of the MnO/N-rGO-800 catalyst in a simulated fuel cell operating conditions as discussed below.

3.3 Fuel cell performance and durability evaluation

It is essential to assess the applicability of non-precious catalysts in a real fuel cell configuration for its practical prospects. Although handful of literatures available on ORR activity of non-precious metal catalyst, mostly their assessments are limited to the liquid electrolyte system studies and their practical applicability in real fuel cell environment are seldom reported. The MnO/N-rGO-800 catalyst developed in this study is not only limited to the ORR activity evaluation in half-cell mode, efforts were also taken to fabricate MEAs and estimate their power density in a real operating fuel cell condition. The polarization and power density curves obtained from a H_2/O_2 single cell test of MEAs comprising MnO/N-rGO-800 (catalyst loading: 6 mg cm^{-2}) and Pt/C (catalyst loading: 2.5 mg cm^{-2}) as cathode catalyst are shown in Fig. 12. As anode catalyst, Pt/C (catalyst loading 2.5 mg cm^{-2}) was used for all single cell studies and hence any variation in performance of a single cell is attributed to the ORR on the cathode catalyst. Under similar operating conditions, Pt/C electrocatalyst showed a peak power density of 117 mW cm^{-2} at a load current density of 245 mA cm^{-2} at 40 °C and ambient pressure. Whereas, MnO/N-rGO-800 electrocatalyst showed peak power density of 44 mW cm^{-2} at a load current density of 94 mA cm^{-2}. It is obvious that, the fuel cell performance of any non-precious catalysts

which are being developed cannot be compared directly with the same catalyst loading as that of precious Pt/C catalyst, as the former catalysts are not active enough at low metal loading. Hence, high catalyst loadings of non-precious catalysts are generally employed in order to compensate the fuel cell performance [46, 47]. On the other hand, high catalyst loadings of non-precious catalysts can significantly increase the catalyst layer thickness (beyond ~ 100 μm). This creates unacceptable mass transport losses at high current densities, resulting in decreased power density. This issue is one of the major limiting factors for the low power density of non-precious catalysts [48, 49]. Hence, optimization of the catalyst loading, electrode porosity, MEA fabrication technique, and fuel cell operating conditions need to be studied and this will be the future scope of study. Therefore, the achieved peak power density of 44 mW cm^{-2} for MnO/N-rGO-800
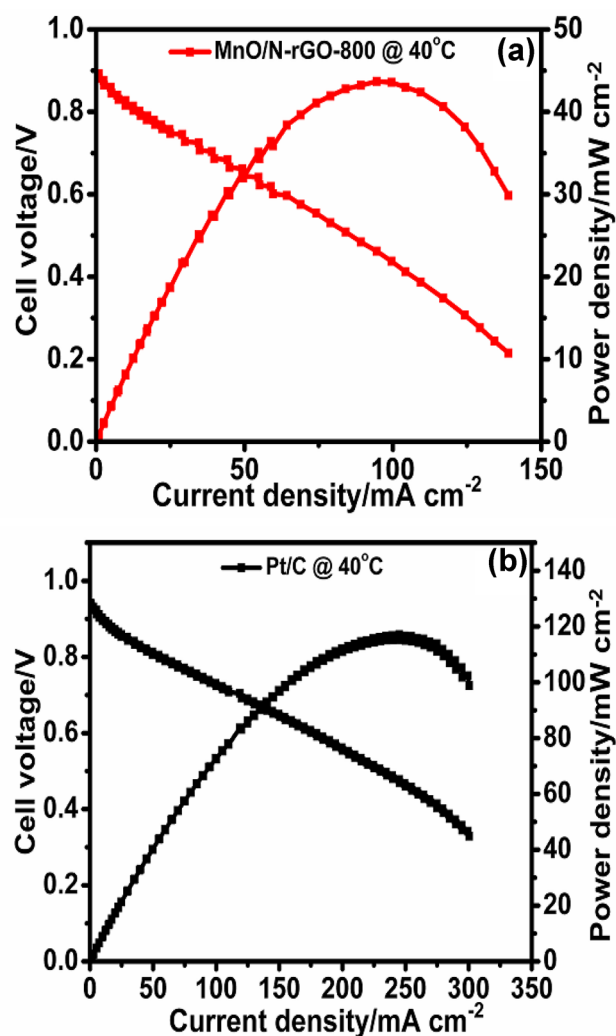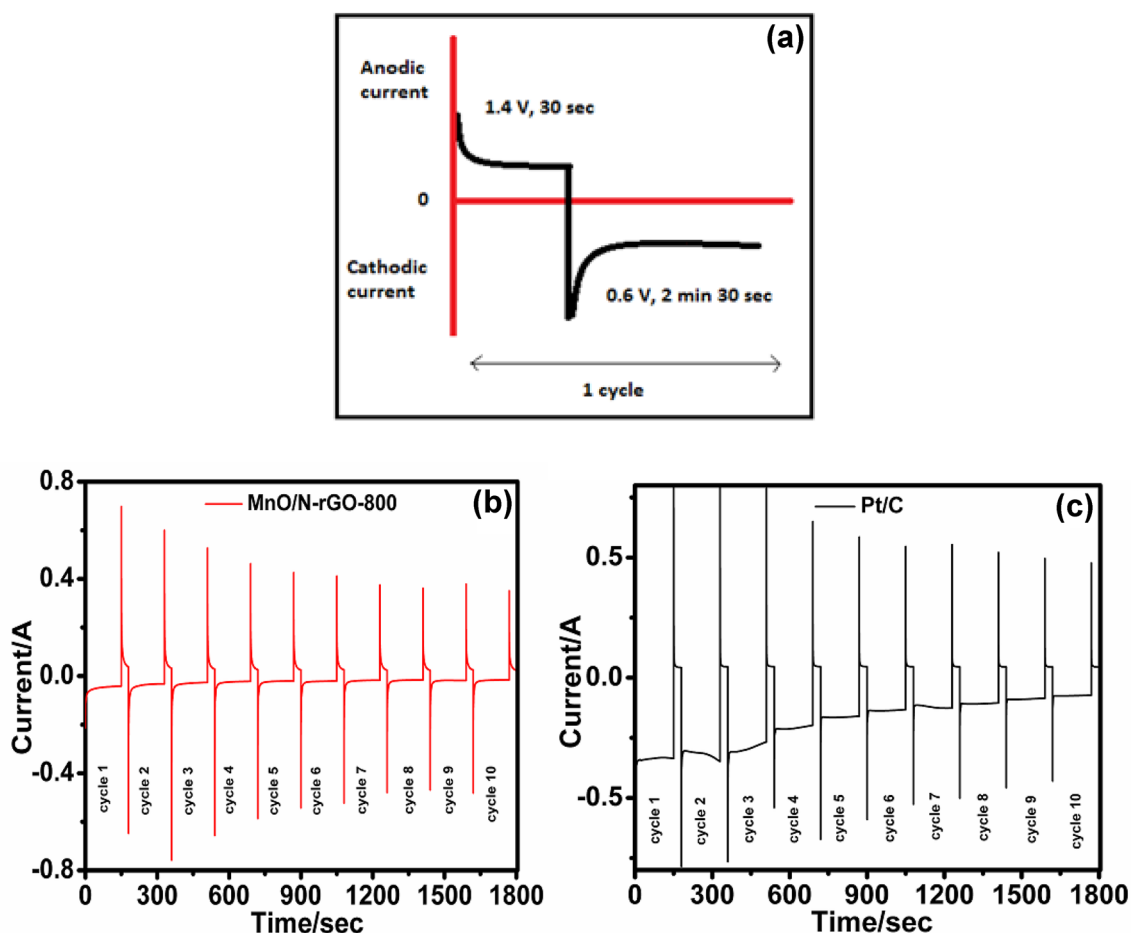
Fig. 12 Polarization and power density curves of AMFC, fabricated with **a** MnO/N-rGO-800 and **b** commercial Pt/C as cathode catalyst in H_2–O_2 feeds at 40 °C and ambient pressure

electrocatalyst is indeed an appreciable improvement as non-precious low cost metal catalyst than the expensive precious Pt catalyst.

The durability of fuel cell MEAs was carried out with an accelerated stress test (AST) method, where the cell was held in two different cell voltage ranges [50] under operating conditions as shown in Fig. 13a. The voltage step with the upper voltage of 1.4 V for 30 s and the lower voltage limits 0.60 V for 2 min 30 s in each cycle was employed and the operating conditions are H_2/O_2 reactants, temperature of 40 °C, 100% RH, and ambient pressure. The upper voltage limit was chosen to be 1.4 V due to the following considerations: (i) 1.4 V is close to the AFC fuel cell cathode voltage in the condition of the reverse current [51] and local fuel starvation [52, 53], start-up and shut-down phenomenon at which the corrosion of electrode support is severe, (ii) 1.4 V is almost the highest voltage without causing any oxygen evolution, otherwise the oxygen evolution gas might mechanically detach catalyst particles from the electrode. The lower voltage limit of 0.6 V is close to the cathode

voltage of normally working AFC fuel cells. By comparing the performance of the MEAs, the degradation information about the electrocatalysts and their support materials can be obtained [50, 54]. The single cell durability performance was evaluated before and after cycling test comprising 50 cycles. Pt/C electrocatalyst contained MEA degraded faster under voltage step conditions than MnO/N-rGO-800-based MEA. MnO-N-rGO-800 cathode catalyst MEA losses were only 27% in peak power density (shown in Fig. 14a) compared to Pt/C cathode catalyst MEA, which showed 83% loss in peak power density after completion of 50 cycles (shown in Fig. 14b). Careful observation of polarization curves of Pt/C after the stability test, one can infer that the over potential in the activation region of the Pt/C catalyst is remarkably high, indicating its poor durability under harsh conditions. This is due to the sensitive Vulcan carbon support, which undergoes severe corrosion resulting in Pt nanoparticle agglomeration and loss of Pt electrochemical active surface area and hence decays in the fuel cell performance as reported by Zadick et al. [55]. In contrast, the polarization

Fig. 13 **a** Pictorial representation of AST mode used for stability test, **b, c** current versus time curve of MnO/N-rGO-800 and Pt/C represented till 10 cycles
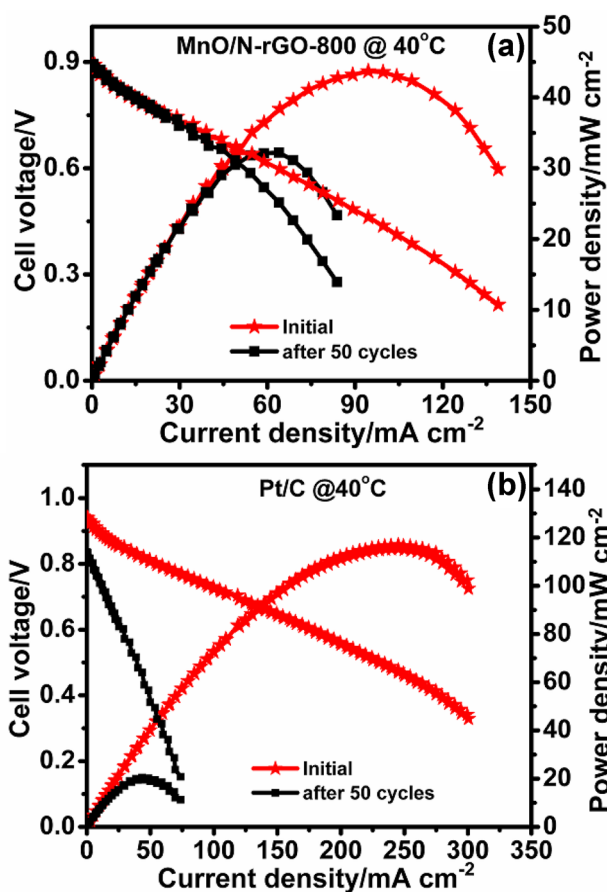
Fig. 14 Polarization and power density curves of AMFC before and after stability test up to 50 cycles fabricated with **a** MnO/N-rGO-800 and **b** commercial Pt/C as cathode catalyst. AMFC cell was feed with H_2–O_2 at 40 °C and ambient pressure

curves of the MnO/N-rGO-800, the activation region of the polarization curve (0.9–0.6 V) does not change even after the stability test. The variation is observed from the Ohmic region of the polarization curve. Thus, the final peak power density in the case of MEAs with MnO/N-rGO-800 as cathode catalyst might be limited by the degradation of alkaline membrane, resulting in the lower hydroxyl ion conductivity. The significant activity and stability of MnO/N-rGO-800 catalyst could be attributed to the synergistic effect between metal oxide/N-rGO hetero-structures and stable N-rGO support. As a result, the MnO/N-rGO-800 catalyst could be an alternative choice of durable cathode catalyst for the AMFC.

4 Conclusion

A non-precious metal electrocatalyst (MnO/N-rGO-800) was successfully synthesized by a simple sol–gel process. Several physical characterizations confirmed that MnO nanoparticles are evenly supported and distributed on the surface of graphene sheets. Electrochemical analysis showed ORR activity of this catalyst is lower than Pt/C; however, durability test of synthesized catalyst showed better performance than Pt/C, wherein, N doping in graphene layers enhances the interaction between the layers and metal oxide particles. The developed MEA with MnO/N-rGO-800 as cathode catalyst in alkaline fuel cells showed an admirable peak power density of 44 mW cm^{-2} at 40 °C and the AST mode stability test of MnO/N-rGO-800-based MEA exhibits superior durability than Pt/C-based MEA. With these performance illustrations, it can be said that a low cost non-precious alternative metal catalyst with improved activity and enhanced durability is developed for the AMFC fuel cell.

References

1. Chen Z, Higgins D, Tao H, Hsu RS, Chen Z (2009) Highly active nitrogen-doped carbon nanotubes for oxygen reduction reaction in fuel cell applications. J Phys Chem C 113:21008–21013. https://doi.org/10.1021/jp908067v
2. Brocq ML, Job N, Eskenazi D, Pireaux JJ (2014) Pt/C catalyst for PEM fuel cells: control of Pt nanoparticles characteristics through a novel plasma deposition method. Appl Catal B 147:453–463. https://doi.org/10.1016/j.apcatb.2013.06.021
3. Shi J, Zhou X, Xu P, Qiao J, Chen Z, Liu Y (2014) Nitrogen and sulfur co-doped mesoporous carbon materials as highly efficient electrocatalysts for oxygen reduction reaction. Electrochim Acta 145:259–269. https://doi.org/10.1016/j.electacta.2014.08.091
4. Higgins DC, Wang R, Hoque MA, Zamani P, Abureden S, Chen Z (2014) Morphology and composition controlled platinum-cobalt alloy nanowires prepared by electrospinning as oxygen reduction catalyst. Nano Energy 10:135–143. https://doi.org/10.1016/j.nanoen.2014.09.013
5. Pan J, Chen C, Zhuang L, Lu J (2012) Designing advanced alkaline polymer electrolytes for fuel cell applications. Acc Chem Res 45:471–483. https://doi.org/10.1021/ar200201x
6. Chung H, Won J, Zelenay P (2013) Active and stable carbon nanotube/nanoparticle composite electrocatalyst for oxygen reduction. Nat Commun 4:1922. https://doi.org/10.1038/ncomms2944
7. Gewirth AA, Thorum MS (2010) Electroreduction of dioxygen for fuel-cell applications materials challenges. Inorg Chem 49:3557. https://doi.org/10.1021/ic9022486
8. Morozan A, Jousselme B, Palacin S (2011) Low-platinum and platinum-free catalysts for the oxygen reduction reaction at fuel cell cathodes. Energy Environ Sci 4:1238. https://doi.org/10.1039/C0EE00601G
9. Chen Y, Wang J, Liu H, Li R, Sun X, Ye S, Knights S (2009) Enhanced stability of Pt electrocatalysts by nitrogen doping in CNTs for PEM fuel cells. Electrochem Commun 11:2071–2076. https://doi.org/10.1016/j.elecom.2009.09.008
10. Borup R, Meyers J, Pivovar B, Kim YS, Mukundan R, Garland N, Myers D, Wilson M, Garzon F, Wood D (2007) Scientific aspects of polymer electrolyte fuel cell durability and degradation. Chem Rev 107:3904–3951. https://doi.org/10.1021/cr050182l
11. Lu Y, Jiang Y, Chen W (2013) PtPd porous nanorods with enhanced electrocatalytic activity and durability for oxygen reduction reaction. Nano Energy 2:836–844. https://doi.org/10.1016/j.nanoen.2013.02.006

12. Zhang J, Guo C, Zhang L, Li L CM (2013) Direct growth of flower-like manganese oxide on reduced graphene oxide towards efficient oxygen reduction reaction. Chem Commun 49:6334. https://doi.org/10.1039/C3CC42127A

13. Ominde N, Bartlett N, Yang XQ, Qu D (2010) Investigation of the oxygen reduction reaction on the carbon electrodes loaded with MnO_2 catalyst. J Power Sources 195:3984. https://doi.org/10.1016/j.jpowsour.2009.12.128

14. Cao S, Han N, Han J, Hu Y, Fan L, Zhou C, Guo R (2016) Mesoporous hybrid shells of carbonized polyaniline/Mn_2O_3 as non-precious efficient oxygen reduction reaction catalyst. ACS Appl Mater Interfaces 8:6040. https://doi.org/10.1021/acsami.5b11955

15. Wu KH, Zeng Q, Zhang B, Leng X, Su DS, Gentle IR, Wang DW (2015) Structural origin of the activity in Mn_3O_4–graphene oxide hybrid electrocatalysts for the oxygen reduction reaction. ChemSusChem 8:3331. https://doi.org/10.1002/cssc.201500372

16. Bag S, Roy K, Gopinath CS, Raj CR (2014) Facile single-step synthesis of nitrogen-doped reduced graphene oxide-Mn_3O_4 hybrid functional material for the electrocatalytic reduction of oxygen. ACS Appl Mater Interfaces 6:2692. https://doi.org/10.1021/am405213z

17. Wu ZS, Yang S, Sun Y, Parvez K, Feng X, Mullen K (2012) 3D nitrogen-doped graphene aerogel-supported Fe_3O_4 nanoparticles as efficient electrocatalysts for the oxygen reduction reaction. J Am Chem Soc 134:9082. https://doi.org/10.1021/ja3030565

18. Guo S, Zhang S, Wu L, Sun S (2012) Co/CoO nanoparticles assembled on graphene for electrochemical reduction of oxygen. Angew Chem Int Ed 51:11770. https://doi.org/10.1002/ange.201206152

19. Odedairo T, Yan X, Ma J, Jiao Y, Yao X, Du A, Zhu Z (2015) Nanosheets Co_3O_4 interleaved with graphene for highly efficient oxygen reduction. ACS Appl Mater Interfaces 7:21373. https://doi.org/10.1021/acsami.5b06063

20. Liu Z, Lin X, Lee J, Zhang W, Han M, Gan L (2002) Preparation and characterization of platinum-based electrocatalysts on multiwalled carbon nanotubes for proton exchange membrane fuel cells. Langmuir 18:4054–4060. https://doi.org/10.1021/la0116903

21. Brock SL, Duan N, Tian ZR, Giraldo O, Zhou H, Suib SL (1998) A review of porous manganese oxide materials. Chem Mater 10:2619–2628. https://doi.org/10.1021/cm980227h

22. Yuan F, Ryu H (2004) The synthesis, characterization, and performance of carbon nanotubes and carbon nanofibres with controlled size and morphology as a catalyst support material for a polymer electrolyte membrane fuel cell. Nanotechnology 15:596–602. https://doi.org/10.1088/0957-4484/15/10/017

23. Steigerwalt E, Deluga G, Cliffel D, Lukehart C (2001) A Pt–Ru/graphitic carbon nanofiber nanocomposite exhibiting high relative performance as a direct-methanol fuel cell anode catalyst. J Phys Chem B 105:8097–8101. https://doi.org/10.1021/jp011633i

24. Chai GS, Yoon SB, Kim JH, Yu J (2004) Spherical carbon capsules with hollow macroporous core and mesoporous shell structures as a highly efficient catalyst support in the direct methanol fuel cell. Chem Commun 23:2766–2767. https://doi.org/10.1039/B412747C

25. Ding J, Chan K, Ren J, Xiao F (2005) Platinum and platinum–ruthenium nanoparticles supported on ordered mesoporous carbon and their electrocatalytic performance for fuel cell reactions. Electrochim Acta 50:3131–3141. https://doi.org/10.1016/j.electacta.2004.11.064

26. Chai GS, Yoon SB, Yu JS (2005) Highly efficient anode electrode materials for direct methanol fuel cell prepared with ordered and disordered arrays of carbon nanofibers. Carbon 43:3028–3031. https://doi.org/10.1016/j.carbon.2005.05.041

27. Benbow EM, Kelly SP, Zhao L, Reutenauer JW, Suib SL (2011) Oxygen reduction properties of bifunctional α-manganese oxide electrocatalysts in aqueous and organic electrolytes. J Phys Chem C 115:22009–22017. https://doi.org/10.1021/jp2055443

28. Peng H, Liu F, Liu X, Liao S, You C, Tian X, Nan H, Luo F, Song H, Fu Z, Huang P (2014) Effect of transition metals on the structure and performance of the doped carbon catalysts derived from polyaniline and melamine for orr application. ACS Catal 4:3797–3805. https://doi.org/10.1021/cs500744x

29. Chetty R, Kundu S, Xia W, Bron M, Schuhmann W, Chirila V, Brandl W, Reinecke T, Muhler M (2009) PtRu nanoparticles supported on nitrogen-doped multiwalled carbon nanotubes as catalyst for methanol electrooxidation. Electrochim Acta 54:4208–4215. https://doi.org/10.1016/j.electacta.2009.02.073

30. Sheng ZH, Shao L, Chen JJ, Bao WJ, Wang FB, Xia XH (2011) Catalyst-free synthesis of nitrogen-doped graphene via thermal annealing graphite oxide with melamine and its excellent electrocatalysis. ACS Nano 5:4350. https://doi.org/10.1021/nn103584t

31. Gong KP, Du F, Xia ZH, Durstock M, Dai LM (2009) Nitrogen-doped carbon nanotube arrays with high electrocatalytic activity for oxygen reduction. Science 323:760. https://doi.org/10.1126/science.1168049

32. Feng J, Liang Y, Wang H, Li Y, Zhang B, Zhou J, Wang J, Regier T, Dai H (2012) Engineering manganese oxide/nanocarbon hybrid materials for oxygen reduction electrocatalysis. Nano Res 5(10):718–725. https://doi.org/10.1007/s12274-012-0256-8

33. She X, Zhang X, Liu J, Li L, Yu X, Huang Z, Shang S (2015) Microwave-assisted synthesis of Mn_3O_4 nanoparticles@reduced graphene oxide nanocomposites for high performance supercapacitors. Mater Res Bull 70:945–950. https://doi.org/10.1016/j.materresbull.2015.06.044

34. Li J, Ren Y, Wang S, Ren Z, Yu J (2016) Transition metal doped MnO_2 nanosheets grown on internal surface of macroporous carbon for supercapacitors and oxygen reduction reaction electrocatalysts. Mater Today 3:63–72. https://doi.org/10.1016/j.apmt.2016.03.003

35. Arunchander A, Vivekanantha M, Peera SG, Sahu AK (2016) MnO–nitrogen doped graphene as a durable non-precious hybrid catalyst for the oxygen reduction reaction in anion exchange membrane fuel cells. RSC Adv 6:95590–95600. https://doi.org/10.1039/C6RA20627A

36. Hummers WS, Offeman RE (1958) Preparation of graphitic oxide. J Am Chem Soc 80:1339–1339

37. Liu C, Li F, Ma LP, Cheng HM (2010) Advanced materials for energy storage. Adv Mater 22:E28. https://doi.org/10.1002/adma.200903328

38. Peera SG, Arunchander A, Sahu AK (2016) Cumulative effect of transition metals on nitrogen and fluorine co-doped graphite nanofibers: an efficient and highly durable non-precious metal catalyst for the oxygen reduction reaction. Nanoscale 8:14650–14664. https://doi.org/10.1039/C6NR02263D

39. Wu Y, Liu S, Wang H, Wang X, Zhang X, Jin G (2013) A novel solvothermal synthesis of Mn_3O_4/graphene composites for supercapacitors. Electrochim Acta 90:210–218. https://doi.org/10.1016/j.electacta.2012.11.124

40. Gautam RK, Bhattacharjee H, Mohan SV, Verma A (2016) Nitrogen doped graphene supported α-MnO_2 nanorods for efficient ORR in a microbial fuel cell. RSC Adv 6:110091–110101. https://doi.org/10.1039/C6RA23392A

41. Lv R, Cui T, Jun MS, Zhang Q, Cao A, Su DS, Zhang Z, Yoon SH, Miyawaki J, Mochida IF. Kang F (2011) Open-ended, N-doped carbon nanotube–graphene hybrid nanostructures as high-performance catalyst support. Adv Funct Mater 21:999–1006. https://doi.org/10.1002/adfm.201001602

42. Park HW, Lee DU, Nazar LF, Chena Z (2013) Oxygen reduction reaction using MnO_2 nanotubes/nitrogen-doped exfoliated graphene hybrid catalyst for Li-O_2 battery

applications. J Electrochem Soc 160(2):A344-A350. https://doi.org/10.1149/2.086302jes

43. Meng Y, Song W, Huang H, Ren Z, Chen SY, Suib SL (2014) Structure–property relationship of bifunctional MnO_2 nanostructures: highly efficient, ultra-stable electrochemical water oxidation and oxygen reduction reaction catalysts identified in alkaline media. J Am Chem Soc 136:11452–11464. https://doi.org/10.1021/ja505186m

44. Tian LL, Yang J, Weng MY, Tan R, Zheng JX, Chen HB, Zhuang QC, Dai LM, Pan F (2017) Fast diffusion of O_2 on nitrogen-doped graphene to enhance oxygen reduction and its application for high-rate Zn–air batteries. ACS Appl Mater Interfaces 9:7125–7130. https://doi.org/10.1021/acsami.6b15235

45. Wu J, Ma L, Yadav RM, Yang Y, Zhang X, Vajtai R, Lou J, Ajayan PM (2015) Nitrogen-doped graphene with pyridinic dominance as a highly active and stable electrocatalyst for oxygen reduction. ACS Appl Mater Interfaces 7:14763–14769. https://doi.org/10.1021/acsami.5b02902

46. Jin Z, Li P, Xiao D (2014) Enhanced electrocatalytic performance for oxygen reduction via active interfaces of layer-by-layered titanium nitride/titanium carbonitride structures. Sci Rep 4:6712–6719. https://doi.org/10.1038/srep06712

47. Li X, Popov BN, Kawahara T, Yanagi H (2011) Non-precious metal catalysts synthesized from precursors of carbon, nitrogen, and transition metal for oxygen reduction in alkaline fuel cells. J Power Sources 196:1717–1722. https://doi.org/10.1016/j.jpowsour.2010.10.018

48. Gasteiger HA, Kocha SS, Sompalli B, Wagner FT (2005) Activity benchmarks and requirements for Pt, Pt-alloy, and non-Pt oxygen reduction catalysts for PEMFCs. Appl Catal B 56:9–35. https://doi.org/10.1016/j.apcatb.2004.06.021

49. Lefèvre M, Proietti E, Jaouen F, Dodelet JP (2009) Iron-based catalysts with improved oxygen reduction activity in polymer electrolyte fuel cells. Science 324:71

50. Shao Y, Kou R, Wang J, Viswanathan VV, Kwak JH, Liu J, Wang Y, Lin Y (2008) The influence of the electrochemical stressing (potential step and potential-static holding) on the degradation of polymer electrolyte membrane fuel cell electrocatalysts. J Power Sources 185:280–286. https://doi.org/10.1016/j.jpowsour.2008.07.008

51. Peera SG, Arunchander A, Sahu AK (2016) Platinum nanoparticles supported on nitrogen and fluorine co-doped graphite nanofibers as an excellent and durable oxygen reduction catalyst for polymer electrolyte fuel cells. Carbon 107:667–679. https://doi.org/10.1016/j.carbon.2016.06.021

52. Knights SD, Colbow KM, Pierre JS, Wilkinson DP (2004) Aging mechanisms and lifetime of PEFC and DMFC. J Power Sources 127:127–134. https://doi.org/10.1016/j.jpowsour.2003.09.033

53. Patterson TW, Darling RM (2006) Damage to the cathode catalyst of a PEM fuel cell caused by localized fuel starvation. Electrochem Solid State Lett 9:A183-A185. https://doi.org/10.1149/1.2167930

54. Shao YY, Yin GP, Gao YZ, Shi PF (2006) Durability study of Pt/C and Pt/CNTs catalysts under simulated PEM fuel cell conditions. J Electrochem Soc 153:A1093-A1097. https://doi.org/10.1149/1.2191147

55. Zadick A, Dubau L, Sergent N, Berthom´e G, Chatenet M (2015) Huge instability of Pt/C catalysts in alkaline medium. ACS Catal 5:4819. https://doi.org/10.1021/acscatal.5b01037

Affiliations

Ila Jogesh Ramala Sarkar[1] · Shaik Gouse Peera[1] · Raghuram Chetty[1]

✉ Raghuram Chetty
raghuc@iitm.ac.in

1 Department of Chemical Engineering, Indian Institute of Technology Madras, Chennai, India